

WISDOM Project – XXIV. Cross-checking supermassive black hole mass estimates from ALMA CO gas kinematics and SINFONI stellar kinematics in the galaxy NGC 4751

Pandora Dominiak,^{1*} Michele Cappellari,¹ Martin Bureau,^{1†} Timothy A. Davis,² Marc Sarzi,³ Ilaria Ruffa,² Satoru Iguchi,^{4,5} Thomas G. Williams¹ and Hengyue Zhang¹

¹*Sub-department of Astrophysics, Department of Physics, University of Oxford, Denys Wilkinson Building, Keble Road, Oxford, OX1 3RH, UK*

²*Cardiff Hub for Astrophysics Research & Technology, School of Physics & Astronomy, Cardiff University, Queens Buildings, Cardiff, CF24 3AA, UK*

³*Armagh Observatory and Planetarium, College Hill, Armagh BT61 9DG, UK*

⁴*Department of Astronomical Science, SOKENDAI (The Graduate University of Advanced Studies), Mitaka, Tokyo 181-8588, Japan*

⁵*National Astronomical Observatory of Japan, National Institutes of Natural Sciences, Mitaka, Tokyo 181-8588, Japan*

Accepted XXX. Received YYY; in original form ZZZ

ABSTRACT

Supermassive black hole (SMBH) masses can be measured by observing the impacts of the SMBHs on dynamical tracers around them. We present high angular resolution (0.19 arcsec or ≈ 24 pc) Atacama Large Millimeter/submillimeter Array observations of the ¹²CO(3–2) line emission of the early-type galaxy NGC 4751, which reveal a highly-inclined regularly-rotating molecular gas disc with clear central Keplerian motions. Using a *Hubble Space Telescope* image to constrain the stellar mass distribution, we forward model the molecular gas kinematics and data cube in a Bayesian framework using the KINEMATIC MOLECULAR SIMULATION code. Assuming a constant mass-to-light ratio (M/L), we infer a SMBH mass $M_{\text{BH}} = 3.43^{+0.45}_{-0.44} \times 10^9 M_{\odot}$ and a $F160W$ filter stellar M/L $M/L_{F160W} = (2.68 \pm 0.11) M_{\odot}/L_{\odot,F160W}$ (all quoted uncertainties are at 3σ confidence). Assuming a linearly spatially-varying M/L , we infer $M_{\text{BH}} = 2.79^{+0.75}_{-0.57} \times 10^9 M_{\odot}$ and $(M/L_{F160W}) / (M_{\odot}/L_{\odot,F160W}) = 3.07^{+0.27}_{-0.35} - 0.09^{+0.08}_{-0.06}$ (R/arcsec), where R is the galactocentric radius. We also present alternative SMBH mass estimates using the Jeans Anisotropic Modelling (JAM) method and Very Large Telescope Spectrograph for INtegral Field Observations in the Near Infrared (SINFONI) stellar kinematics. Assuming a cylindrically-aligned velocity ellipsoid (JAM_{cyl}) we infer $M_{\text{BH}} = (2.52 \pm 0.36) \times 10^9 M_{\odot}$, while assuming a spherically-aligned velocity ellipsoid (JAM_{sph}) we infer $M_{\text{BH}} = (3.24 \pm 0.87) \times 10^9 M_{\odot}$. Our derived masses are all consistent with one another, but they are larger than (and inconsistent with) one previous stellar dynamical measurement using Schwarzschild’s method and the same SINFONI kinematics.

Key words: galaxies: individual: NGC 4751 – galaxies: elliptical and lenticular, cD – galaxies: kinematics and dynamics – galaxies: nuclei – galaxies: ISM

1 INTRODUCTION

Observations over the last three decades have demonstrated that nearly every massive galaxy hosts a supermassive black hole (SMBH) at its centre. These SMBHs dynamically influence only the most central regions of their host galaxies. Despite this, their properties are tightly correlated with those of their hosts (e.g. Magorrian et al. 1998; Kormendy & Ho 2013; McConnell & Ma 2013). The tightest of these correlations is that between SMBH mass (M_{BH}) and stellar velocity dispersion measured within one effective (i.e. half-light) radius (σ_e), commonly referred to as the $M_{\text{BH}} - \sigma_e$ relation (e.g. Gebhardt et al. 2000; Gültekin et al. 2009). These correlations suggest that SMBHs co-evolve with their host galaxies, but the details of the self-regulating processes are still poorly understood.

The ability to study SMBH – host galaxy correlations relies on

accurate methods of SMBH mass determination. The most reliable estimates are obtained by probing matter within the gravitational spheres of influence (SoI) of the SMBHs. These methods thus require high-spatial resolution observations, to discern the impacts of the SMBHs on the matter in the innermost regions of their host galaxies. Whilst a variety of kinematic tracers exist to probe the SMBH SoI, such as stars, ionised gas and megamasers, different methods tend to work best in different types of targets. Stellar kinematic methods have mainly been used in early-type galaxies (ETGs), whereas ionised gas is typically used in late-type galaxies (LTGs), and masers are only present in rather low-mass Seyfert 2 and low-ionisation nuclear emission region (LINER) galaxies. Each of these methods also suffers from distinct systematic weaknesses that might bias the SMBH masses derived. To identify potential inconsistencies between the different methods, it is clear that there is a need to cross-check the SMBH masses obtained using different methods in the same targets. However, such cross-checks have proven to be incredibly challenging due to the limited number of targets suitable for multiple methods of mass

* E-mail: pandora.dominiak@physics.ox.ac.uk

† E-mail: martin.bureau@physics.ox.ac.uk

determination. To date, the SMBH masses of only 11 targets have been cross-checked between stellar, ionised gas, reverberation mapping and maser methods (see [Liang et al. 2023](#) for a summary).

In recent years, a new method of SMBH mass determination has emerged that utilises molecular gas as the kinematic tracer. Molecular gas is a particularly good dynamical tracer as it can be detected in a wide variety of galaxies along the Hubble sequence (even those that are no longer star forming) and is unaffected by dust. This method has been used most often in typical ETGs ([Davis et al. 2013b](#); [Barth et al. 2016](#); [Davis et al. 2017a](#); [Onishi et al. 2017](#); [Davis et al. 2017b](#); [Nagai et al. 2019](#); [Boizelle et al. 2019](#); [North et al. 2019](#); [Smith et al. 2019](#); [Ruffa et al. 2019](#); [Davis et al. 2020](#); [Cohn et al. 2021](#); [Smith et al. 2021](#); [Boizelle et al. 2021](#); [Kabasares et al. 2022](#); [Ruffa et al. 2023](#); [Dominiak et al. 2024](#); [Zhang et al. in prep.](#)), but it has also been used in three LTGs (all barred spirals; [Onishi et al. 2015](#); [Nguyen et al. 2020](#); [Nguyen et al. 2021](#)), a dwarf ETG ([Davis et al. 2020](#)) and a peculiar luminous infrared galaxy (LIRG) with central spiral arms ([Lelli et al. 2022](#)).

The variety of targets in which this method can be utilised makes molecular gas SMBH mass measurements promising candidates for cross-checks. Thus far molecular gas has enabled the following cross-checks in 7 objects, increasing the number of cross-checked masses by two thirds: (i) ‘molecular gas vs. ionised gas’ in NGC 4261 ([Ferrese et al. 1996](#); [Boizelle et al. 2021](#)) and NGC 7052 ([van der Marel & van den Bosch 1998](#); [Smith et al. 2021](#)) and (ii) ‘molecular gas vs. stars’ in NGC 524 ([Krajinović et al. 2009](#); [Smith et al. 2019](#)), NGC 1332 ([Rusli et al. 2010](#); [Barth et al. 2016](#)), NGC 4697 ([Schulze & Gebhardt 2011](#); [Davis et al. 2017a](#)), NGC 6861 ([Rusli et al. 2013](#); [Kabasares et al. 2022](#)) and the dwarf galaxy NGC 404 ([Nguyen et al. 2017](#); [Davis et al. 2020](#)).

This paper presents observations and kinematic modelling of the $^{12}\text{CO}(3-2)$ line emission of the ETG NGC 4751, observed at high angular resolution with the Atacama Large Millimeter/submillimeter Array (ALMA). NGC 4751 already has a SMBH mass determined using Schwarzschild models of its stellar kinematics ([Rusli et al. 2013](#)), but in this paper we also present an alternative stellar kinematic SMBH mass estimate using the same data as [Rusli et al. \(2013\)](#) but the Jeans Anisotropic Modelling (JAM) method ([Cappellari 2008](#); [Cappellari 2020](#)). Not only will these new measurements allow us to add NGC 4751 to the growing list of SMBH masses cross-checked between the molecular gas and stellar kinematic methods, but it will also allow us to compare SMBH masses determined using different stellar kinematic modelling methods.

This paper is structured as follows. In Section 2 we summarise the main properties of the target, NGC 4751. The ALMA data, their reduction and the properties of the resulting CO data cube and continuum emission are described in Section 3. We describe and present the results of the molecular gas dynamical modelling in Section 4. We present the alternative SMBH mass measurements using stellar kinematics in Section 5. We discuss these results within the context of other SMBH mass measurements in the literature in Section 6, and summarise and conclude in Section 7.

2 NGC 4751

NGC 4751 is an ETG located at $12^{\text{h}}52^{\text{m}}50^{\text{s}}.79$, $-42^{\circ}39'35''.7$ (J2000.0). Throughout this paper we adopt a distance $D = 26.9$ Mpc, that was calculated using the galaxy heliocentric velocity corrected for infall of the Local Group into the Virgo Cluster of galaxies and assuming a Hubble constant $H_0 = 72$ km s $^{-1}$ Mpc $^{-1}$ ([Rusli et al. 2013](#)). At this distance, 1 arcsec corresponds to ≈ 130 pc.

NGC 4751 has a total absolute B band magnitude of -19.71 and a total absolute V band magnitude of -20.75 ([Rusli et al. 2013](#)). Based on Two Micron All Sky Survey K_s filter images, it has a spheroid absolute magnitude of -21.53 ± 0.60 and a total absolute magnitude of -22.11 ± 0.20 ([Sahu et al. 2019](#)). Based on these and a stellar mass-to-light ratio of $0.7 M_{\odot}/L_{\odot,3.6\mu\text{m}}$ ([Sahu et al. 2019](#)), NGC 4751 has an estimated spheroid stellar mass $M_{\star,\text{sph}} = 3.09^{+2.53}_{-1.39} \times 10^{10} M_{\odot}$ and an estimated total galaxy stellar mass $M_{\star,\text{gal}} = 5.25^{+1.67}_{-1.27} \times 10^{10} M_{\odot}$ ([Sahu et al. 2019](#)).

Hubble Space Telescope (HST) optical images reveal a prominent nearly edge-on dust disc, ≈ 34 arcsec in diameter along its major axis, with dust lanes to the west of an unobscured nucleus (see Fig. 1). There is a small object ≈ 18 arcsec south of NGC 4751, most likely a foreground star (Fig. 1).

There is some disagreement as to whether NGC 4751 is an elliptical or a lenticular galaxy. Images of NGC 4751 suggest that it is comprised of two components, a relatively round central component with a steep radial surface brightness profile and an outer component that is flatter and has a shallower surface brightness profile. This is a defining characteristic of S0 galaxies, and if the central component is interpreted as a bulge and the outer component as a disc, the bulge-to-total luminosity ratio $B/T = 0.55 \pm 0.05$ ([Kormendy & Ho 2013](#)). Thus, canonically-speaking, NGC 4751 should be classified as an S0 galaxy. However, some studies suggest that both cluster ([Kormendy et al. 2009](#)) and field ([Huang et al. 2013](#)) ellipticals are naturally divided into objects that have cores (formed through dry mergers) and objects that have extra central light (formed through wet mergers). Thus, [Kormendy & Ho \(2013\)](#) argue that NGC 4751 is really a highly-flattened extreme (E6) extra-light elliptical galaxy, whereby the central component is interpreted as resulting from a starburst event and the outer component is the consequence of the violent relaxation of pre-existing stars ([Mihos & Hernquist 1994](#); [Hopkins et al. 2009](#)).

Integral-field spectroscopic data obtained using adaptive optics-assisted SINGLe Faint Object Near-IR Investigation (SINFONI) observations on the Very Large Telescope were modelled using three-integral Schwarzschild models by [Rusli et al. \(2013\)](#) to infer a central SMBH mass $M_{\text{BH}} = (1.4 \pm 0.1) \times 10^9 M_{\odot}$ and a stellar mass-to-light ratio (M/L) in the R band $M/L_R = 12.2^{+0.6}_{-0.7} M_{\odot}/L_{\odot,R}$ (based on a model with dark matter present) or $M/L_R = 13.1^{+0.3}_{-0.4} M_{\odot}/L_{\odot,R}$ (based on a model without dark matter).

NGC 4751 has an effective radius $R_e = 22.8$ arcsec, a central velocity dispersion $\sigma_0 = 357.6 \pm 17.7$ km s $^{-1}$ ([Campbell et al. 2014](#)) and an effective stellar velocity dispersion $\sigma_e = 355.4 \pm 13.6$ km s $^{-1}$ ([Rusli et al. 2013](#)). Using the latter and the $M_{\text{BH}} - \sigma_e$ relation of [van den Bosch \(2016\)](#), we expect a SMBH mass of $\approx 4.5 \times 10^9 M_{\odot}$, about three times larger than that inferred by [Rusli et al. \(2013\)](#). The radius of a SMBH’s sphere of influence (R_{SOI}) quantifies the spatial extent over which the gravitational potential of the SMBH is dominant. One way to calculate this is through $R_{\text{SOI}} \equiv GM_{\text{BH}}/\sigma_e^2$, where G is the gravitational constant. Using the SMBH mass of [Rusli et al. \(2013\)](#) yields $R_{\text{SOI}} \approx 48$ pc (≈ 0.37 arcsec), whereas the SMBH mass estimate from the $M_{\text{BH}} - \sigma_e$ relation yields $R_{\text{SOI}} \approx 154$ pc (≈ 1.18 arcsec).

3 ALMA OBSERVATIONS

Observations of the $^{12}\text{CO}(3-2)$ emission line of NGC 4751 using the 12-m ALMA array in band 7 were obtained as part of project 2016.1.01135.S (PI: Nagar). The data were collected with one track

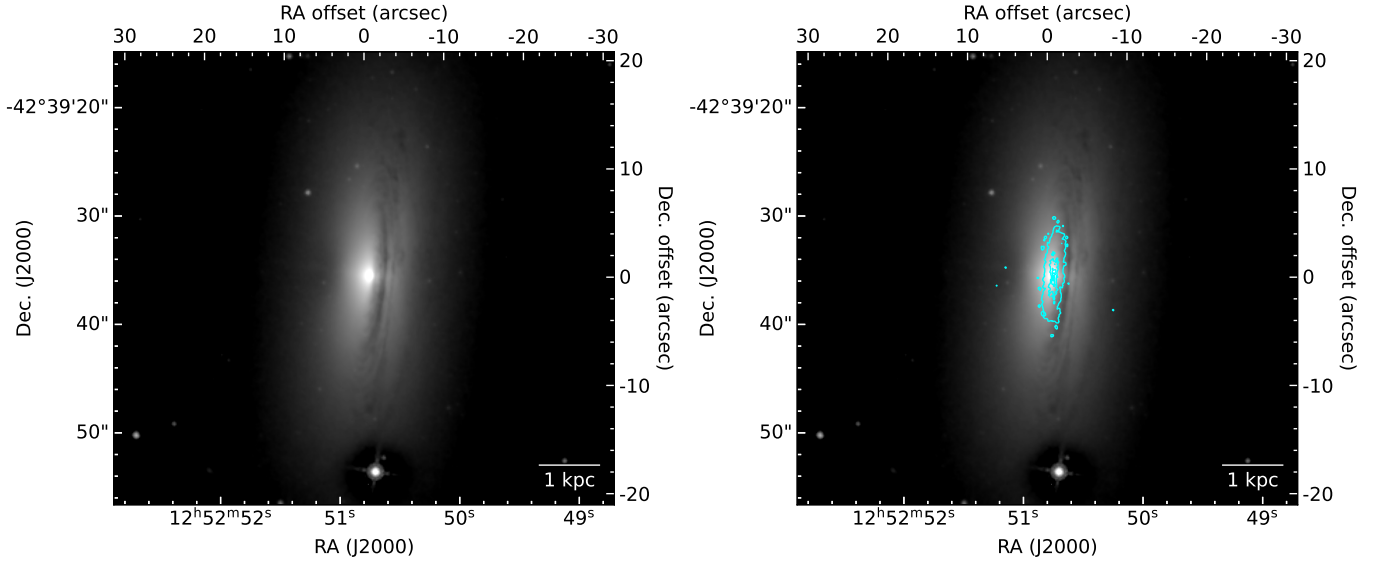


Figure 1. Unsharp-masked *HST* Wide Field Camera 3 *F160W* filter (*H* band) image of NGC 4751 (left), overlaid with the $^{12}\text{CO}(3-2)$ integrated-intensity contours (cyan) from our ALMA observations (right).

on 2017 May 17, for a total of 1361 s on source. The baselines range from 15 m to 1.1 km, yielding spatial resolutions of 0.19 arcsec (≈ 25 pc) to 14.5 arcsec (≈ 1.9 kpc), a maximum recoverable scale of 2.2 arcsec (≈ 290 pc) and a field of view of 16.7 arcsec (≈ 2.2 kpc).

The observations had four spectral windows, each with a bandwidth of 2.0 GHz (≈ 1735 km s $^{-1}$) subdivided into 128 channels of ≈ 16 MHz (≈ 13.5 km s $^{-1}$). Two of the spectral windows were centred on both sides of the redshifted frequency of the $^{12}\text{CO}(3-2)$ line (rest frequency $\nu_{\text{rest}} = 345.7959899$ GHz), with a small gap in frequency between them. The remaining two spectral windows were used to map the continuum. The data were calibrated using the COMMON ASTRONOMY SOFTWARE APPLICATIONS (CASA) package version 4.7.2 (McMullin et al. 2007) and the standard ALMA pipeline. The following imaging steps used CASA version 6.4.3.

3.1 Line emission

The continuum spectral windows and line-free channels of the line spectral windows were linearly fit and the fit was then subtracted from the data in the *uv*-plane using the CASA task *uvcontsub*. The continuum-subtracted *uv* data were then imaged and cleaned interactively to a threshold equal to the root-mean-square (RMS) noise of the dirty channels (measured in regions free of line emission), using the CASA task *tclean* and Briggs weighting with a robust parameter of 0.5 and a channel width of 30 km s $^{-1}$. The resulting data cube has a synthesised beam of 0.20 arcsec \times 0.18 arcsec ($\approx 26 \times 23$ pc 2), sampled with 4–5 spaxels linearly, and a RMS noise of 0.44 mJy beam $^{-1}$ channel $^{-1}$. The properties of the data cube are summarised in Table 1.

Zerth (integrated-intensity), first (intensity-weighted mean line-of-sight velocity) and second (intensity-weighted line-of-sight velocity dispersion) moment maps were created using a standard masked-moment technique (Dame 2011) implemented in the PYMAKEPLOTS package¹. The CO data cube without primary-beam correction is

Table 1. CO data cube properties.

Property	Value
Spatial extent (pix)	800 \times 800
Spatial extent (arcsec)	32.0 \times 32.0
Spatial extent (kpc)	4.2 \times 4.2
Pixel scale (arcsec pix $^{-1}$)	0.04
Pixel scale (pc pix $^{-1}$)	5.2
Velocity range (km s $^{-1}$)	1300 – 2800
Channel width (km s $^{-1}$)	30
RMS noise (mJy beam $^{-1}$ channel $^{-1}$)	0.44
Number of constraints	86,091
Synthesised beam (arcsec)	0.20 \times 0.18
Synthesised beam (pc)	26 \times 23

first boxcar-smoothed in the spatial and spectral dimensions, with a spatial kernel of 1.5 times the width of the synthesised beam and a spectral kernel of 4 times the channel width. A binary mask is then created by clipping this smoothed data cube at a threshold of 5 times the RMS noise of the line-free channels of the same smoothed cube. The moment maps and the position-velocity diagram (PVD) below are then created by applying this mask to the unsmoothed primary beam-corrected (i.e. the original) data cube. A kinematic major-axis PVD was created by taking a cut through the masked cube at a position angle of 354 $^{\circ}$.8. The resulting moment maps and PVD are shown in Fig. 2.

We detect a highly-inclined disc of molecular gas, ≈ 9 arcsec \times 2 arcsec in projection, in regular rotation and coincident with but much smaller than the dust disc (see Fig. 1). Contrary to other galaxies with observations at similar spatial resolutions (Davis et al. 2022), the molecular gas of NGC 4751 extends all the way to the centre, with no circumnuclear hole nor clear depression. The vast majority of existing molecular gas SMBH measurements used lower-*J* transitions, most commonly $^{12}\text{CO}(2-1)$. The lack of a central hole in our $^{12}\text{CO}(3-2)$ data may thus indicate that thermal effects in accretion discs reduce the fraction of gas emitting in the low-*J* transitions in the innermost regions. The PVD shows a rotation curve with a remarkably extended Keplerian decline in the centre.

¹ <https://github.com/TimothyADavis/pymakeplots>

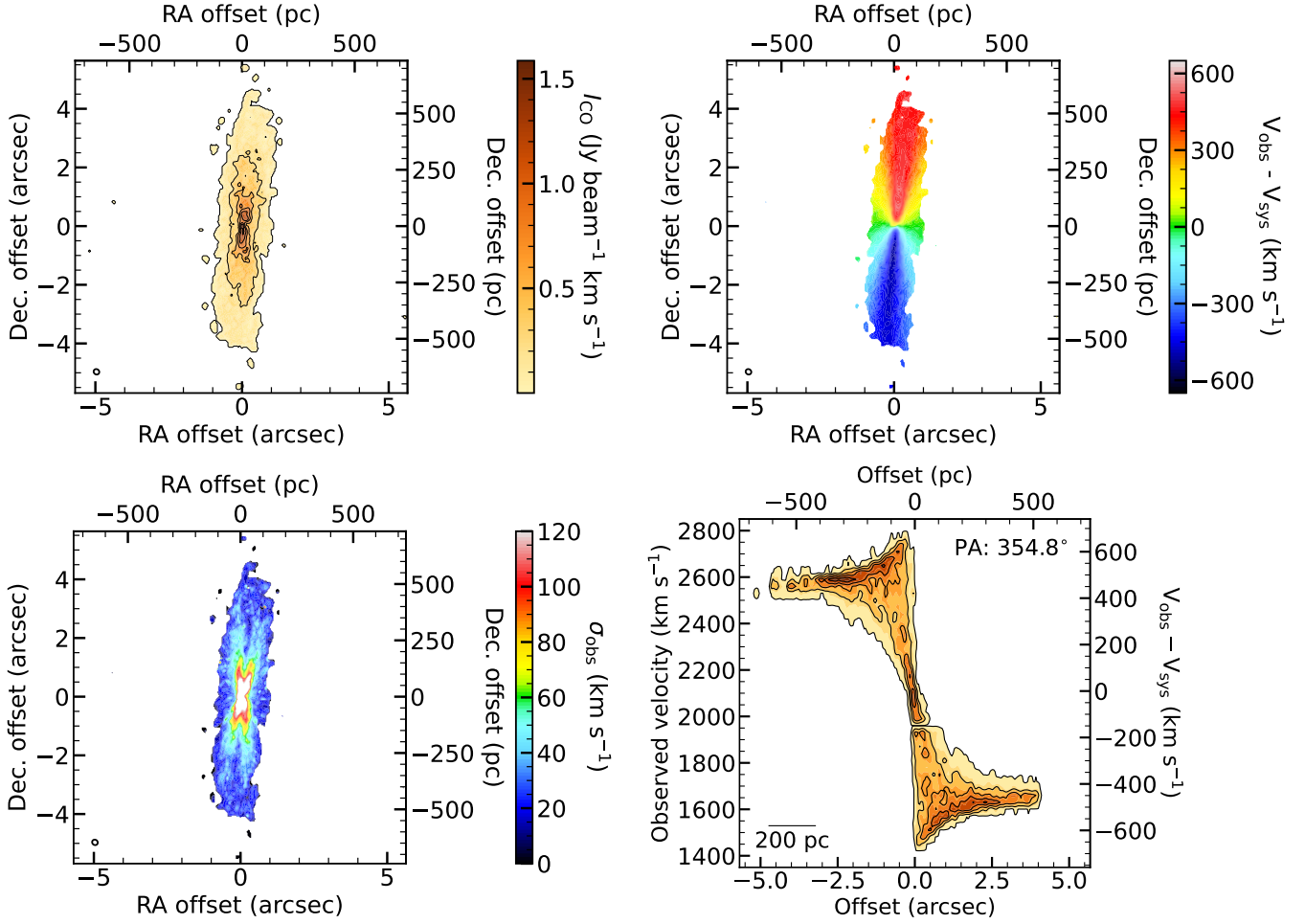


Figure 2. $^{12}\text{CO}(3-2)$ data products of NGC 4751 derived from our ALMA data. **Top-left:** zeroth-moment (integrated-intensity) map. **Top-right:** first-moment (intensity-weighted mean line-of-sight velocity) map. **Bottom-left:** second-moment (intensity-weighted line-of-sight velocity dispersion) map. **Bottom-right:** kinematic major-axis position-velocity diagram. The synthesised beam is shown in the bottom-left corner of each map as an open ellipse. A scale bar is shown in the bottom-left corner of the PVD.

Figure 3 shows the $^{12}\text{CO}(3-2)$ integrated spectrum of NGC 4751, with the characteristic double-horn shape of a rotating disc. This spectrum was extracted from a $6 \text{ arcsec} \times 6 \text{ arcsec}$ ($\approx 780 \times 780 \text{ pc}^2$) region around the centre of the galaxy, with an integrated flux (measured within the mask defined above) of $80.5 \pm 0.2 \text{ Jy km s}^{-1}$. This includes emission in the missing channels, which was interpolated linearly from the closest channels on either side. Assuming a $^{12}\text{CO}(3-2)/^{12}\text{CO}(1-0)$ line ratio of 0.31 (in brightness temperature units; Leroy et al. 2022) and a standard $\text{CO}(1-0)$ -to-molecule conversion factor (with contribution from heavy elements included) $\alpha_{\text{CO}(1-0)} = 4.35 \text{ M}_{\odot} \text{ pc}^{-2} (\text{K km s}^{-1})^{-1}$, we obtain a $\text{CO}(3-2)$ -to-molecule conversion factor $\alpha_{\text{CO}(3-2)} = 14.0 \text{ M}_{\odot} \text{ pc}^{-2} (\text{K km s}^{-1})^{-1}$, yielding a total molecular gas mass of $(2.27 \pm 0.01) \times 10^8 \text{ M}_{\odot}$.

3.2 Continuum emission

An image of the continuum emission of NGC 4751 was created using the *CASA* task `tclean` in multi-frequency synthesis mode and Briggs weighting with a robust parameter of 0.5, with a central frequency of 343.5 GHz (0.87 mm). The line-free channels of the line spectral windows were used as well as the continuum spectral windows, resulting in a RMS noise of $0.07 \text{ mJy beam}^{-1}$. A small

Table 2. Parameters of the NGC 4751 continuum image and the detected continuum source.

Image property	Value
Image (pix)	800×800
Image (arcsec)	32×32
Image size (kpc)	4.2×4.2
Pixel scale (arcsec pix $^{-1}$)	0.04
Pixel scale (pc pix $^{-1}$)	5.2
RMS noise (mJy beam $^{-1}$)	0.07
Synthesised beam (arcsec)	0.19×0.17
Synthesised beam (pc)	25×22
Source property	Value
Right ascension (J2000.0)	$12^{\text{h}}52^{\text{m}}50^{\text{s}}.7445 \pm 0^{\text{s}}.0002$
Declination (J2000.0)	$-42^{\circ}39'35''.545 \pm 0''.002$
Integrated flux (mJy)	8.81 ± 0.34
Deconvolved size (marsec)	$< 78 \times 19$
Deconvolved size (pc)	$< 10 \times 2$

central source was detected and fitted with a Gaussian function using the *CASA* task `imfit`, revealing a spatially-unresolved source with an integrated flux density of $8.81 \pm 0.34 \text{ mJy}$. The properties of the continuum image and the detected source are listed in Table 2.

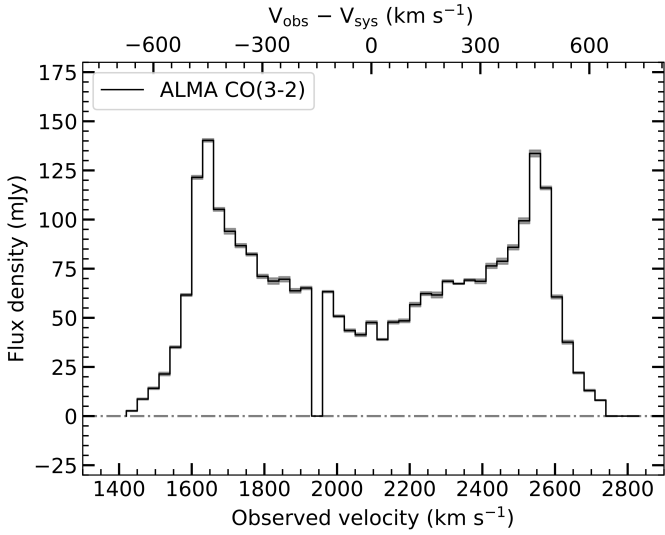


Figure 3. $^{12}\text{CO}(3-2)$ integrated spectrum of NGC 4751, with the characteristic double-horn shape of a rotating disc. Uncertainties are shown as grey shading. The spectrum was extracted from a $6 \text{ arcsec} \times 6 \text{ arcsec}$ ($\approx 780 \times 780 \text{ pc}^2$) region centred on the galaxy centre, that includes all detected emission. The data were obtained in two spectral windows which do not overlap in velocity, hence the small gap at $\approx 1940 \text{ km s}^{-1}$.

4 DYNAMICAL MODELLING OF CO GAS KINEMATICS

4.1 Modelling method

Dynamical modelling is carried out by fitting a model to the observed molecular gas distribution and kinematics, i.e. the data cube discussed in the previous section. This method of SMBH mass determination has been used in other papers of this series (e.g. Davis et al. 2017a; Smith et al. 2021; Ruffa et al. 2023).

First we need to model the molecular gas distribution of the galaxy. Due to its simple morphology, we can reproduce the molecular gas distribution of NGC 4751 with an infinitely-thin (i.e. two-dimensional, 2D) axisymmetric exponential surface brightness profile (known to often be appropriate for ETGs; e.g. Davis et al. 2013a; Ruffa et al. 2019), parameterised as

$$I(R) \propto e^{-R/R_0}, \quad (1)$$

where R is the galactocentric radius and R_0 the exponential scale length, the latter being a free parameter of our model. This surface density profile is then scaled to match the integrated $^{12}\text{CO}(3-2)$ flux, leading to another free parameter of our model.

Our model also takes into account the velocity dispersion of the molecular gas (σ_{gas}), which is another free parameter of our model. This velocity dispersion is assumed to be spatially constant and small relative to the rotational velocities, as is typically observed in nearby, dynamically-cold molecular gas discs ($\sigma_{\text{gas}} \lesssim 20 \text{ km s}^{-1}$; e.g. Davis et al. 2017a, North et al. 2019).

Second, to estimate the SMBH mass accurately, we must account for the stellar mass contribution to the gravitational potential. In principle dark matter should also be considered, but at the small radii probed here the dark matter contribution is expected to be negligible (it would in any case be largely degenerate with that of the stars; Cappellari et al. 2013). We parameterise the stellar light distribution using a multi-Gaussian expansion (MGE) model of a *HST* Wide Field Camera 3 (WFC3) *F160W* filter (*H* band) image. For this,

Table 3. Parameters of the deconvolved best-fitting MGE components.

I'_0 ($L_{\odot, F160W} \text{ pc}^{-2}$)	σ' (arcsec)	q'
(1)	(2)	(3)
310086	0.153	0.647
70882	0.378	0.494
27597	0.578	0.990
14135	1.481	0.750
12562	1.502	0.319
10044	3.344	0.517
3244	8.596	0.397
819	25.788	0.420

Notes. Deconvolved MGE Gaussian components. (1) Central surface brightness. (2) Standard deviation. (3) Axial ratio.

we use the `mge_fit_sectors` procedure in the `MGEfit` package² (Cappellari 2002). This is the longest wavelength *HST* image available, to minimise dust extinction. We use the `TINYTIM` code (Krist et al. 2011) to calculate the spatial point-spread function (PSF) of the filter, and parameterise it by fitting it with a circular MGE model, using the same `MGEfit` package as above.

The 2D projection of the stellar light distribution captured by the *HST* image is parameterised by the MGE as a sum of Gaussians, each with a central surface brightness I , a width σ and an axial ratio q . The surface brightnesses can be converted into luminosities using the AB magnitude system with a zero-point of 25.94 mag (Sahu et al. 2021) and a Solar absolute magnitude of 4.60 mag (Willmer 2018). Additionally, we adopt a galactic extinction of 0.062 mag from the NASA/IPAC Extragalactic Database (Schlafly & Finkbeiner 2011) to correct for interstellar reddening. The parameters of the deconvolved best-fitting MGE Gaussians are listed in Table 3 in physical units and the fit is shown in Fig. 4. As can be seen in Fig. 4, there is significant dust extinction to the west of the NGC 4751 nucleus. To reduce their impact, the dust lanes were therefore masked in our MGE model, simultaneously masking the nearby galaxy to the south (not seen in Fig. 4). The resulting MGE model is clearly a good fit, especially in the very centre of the image, the region that matters most to constrain the SMBH mass.

Given an inclination, which is another free parameter of our model, the 2D MGE surface brightness model can be analytically deprojected into a three-dimensional (3D) light volume density distribution. The deprojection is generally mathematically non-unique (e.g. Gerhard & Binney 1996) even in axisymmetry, unless the galaxy is edge-on. However, given the near edge-on inclination of NGC 4751, the degeneracy is likely small. We deproject under the MGE assumptions (Cappellari 2002). The 3D light volume density distribution can then be converted into a 3D stellar mass volume density distribution by simply multiplying each Gaussian component by a stellar M/L , which is another free parameter of our model. This M/L is usually assumed to be spatially constant, but in this paper we will also consider a M/L varying linearly with radius. This is achieved by taking the circular velocity curve derived from our MGE model assuming a M/L of unity ($1 M_{\odot}/L_{\odot, H}$) and scaling that curve by the square root of the variable M/L (as circular velocities are proportional to the square root of the enclosed masses). In such a case, the M/L intercept and M/L gradient are free parameters of our model instead. The stellar mass model and the (free) SMBH mass are then used with the `mge_vcirc` routine of the `JEANS ANISOTROPIC`

² <https://pypi.org/project/mgefit/>

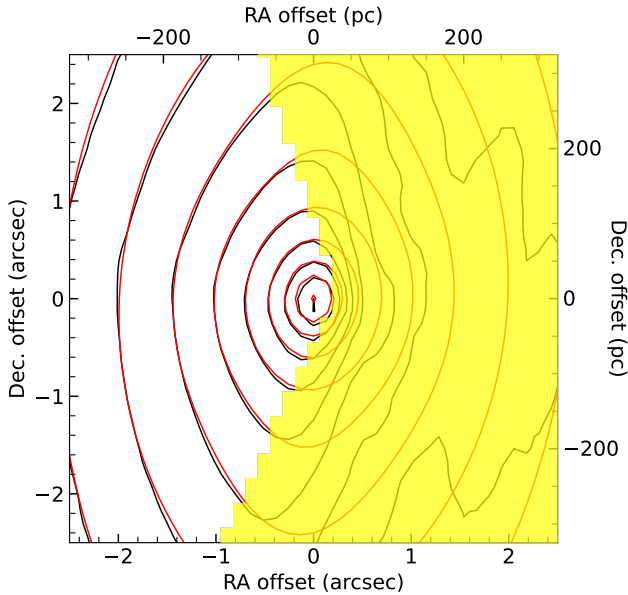


Figure 4. *HST* WFC3 *F160W* filter image of NGC 4751 (black contours), overlaid with our best-fitting MGE model (red contours). The western side of the image is masked (yellow shading), to exclude the foreground dust disc and contamination from a nearby star.

MODELLING Python package (JAMPY³; Cappellari 2008; Cappellari 2020) to calculate the associated circular velocity curve.

By combining the molecular gas distribution and the circular velocity curve obtained above, the KINEMATIC MOLECULAR SIMULATION (KINMS; Davis et al. 2013a) task `KinMS_fitter`⁴ simulates the molecular gas disc as a collection of point particles. These are then used to create a model data cube by calculating their line-of-sight projections, taking into account the position (spatial centre and systemic velocity), inclination and position angle (both assumed to be radially constant) of the galaxy, all of which are free parameters of the model. To replicate instrumental effects, this cube is then spatially convolved with the Gaussian synthesised beam and (spatially and spectrally) binned into pixels identical to those of the real data cube.

We use the Gibbs sampler with adaptive stepping GASTIMATOR⁵ to compare our model and ALMA data cubes. Initially, the Monte Carlo Markov chain (MCMC) algorithm samples the parameter space of all the free parameters of the model, and the step size between each fit is adaptively scaled until the chain converges. This initial burn-in phase to identify the convergent chain comprises ≈ 10 per cent of the total number of steps. Once the MCMC has converged, the maximum step size is fixed and the MCMC keeps sampling the parameter space, generating samples from the final posterior probability distribution.

The parameter space is bounded by a set of priors. Some are set manually to ensure a finite converging time; others are allowed to span their entire possible ranges. The priors for all the parameters are linear, except for that on the SMBH mass which is logarithmic due to its large dynamic range. Assuming these maximally-ignorant priors and constant Gaussian uncertainties throughout the cube, the posterior probability distribution of a model is proportional to the log-likelihood function $\ln P \propto -0.5\chi^2$, where χ^2 is defined in the standard manner

³ <https://pypi.org/project/jampy>

⁴ https://github.com/TimothyADavis/KinMS_fitter

⁵ <https://github.com/TimothyADavis/GASTimator>

as the sum (over all all pixels of the cube) of the differences between model and data squared normalised by the uncertainties squared. We rescale the uncertainties of the cube by a factor of $(2N)^{0.25}$, where N is the number of constraints (i.e. the number of pixels with detected emission, as defined by the mask in Section 3.1 and listed in Table 1), to ensure that the large N does not lead to unrealistically small formal uncertainties. This approach was originally proposed by van den Bosch & van de Ven (2009) for use in least-squares fitting and adapted to the Bayesian framework by Mitzkus et al. (2017). It is not statistically rigorous, but tries to approximately account for the fact that systematic uncertainties tend to dominate the total uncertainties when fitting a large number of measurements (thousands). It relies on the sensible but crude assumption that each random uncertainty has an associated systematic one of similar magnitude. In the case of BH determinations from CO, the method has been shown to generally yield uncertainties that are consistent with more realistic estimates of the systematic uncertainties (Smith et al. 2019).

Each of the free parameters of our model undergoes a process of marginalisation as part of the MCMC chain. The probability distributions of each parameter against the others are shown as 2D marginalisations in Figs. 5 and 6, where each data point represents the log-likelihood of a model (white data points are most likely, blue data points least likely). The posterior probability distributions of the individual parameters are also shown as one-dimensional (1D) marginalisations (i.e. histograms). All these histograms are roughly Gaussian in shape, indicating that the chains have converged.

4.2 Results

Throughout our modelling we have considered models with various M/L profiles. The spatially-constant and radially linearly-varying M/L models yield equally good fits, so the results of both are presented below. Other M/L assumptions are briefly discussed in Section 6.3.

4.2.1 Model with constant M/L

This model has a total of 10 free parameters: SMBH mass (M_{BH}), spatially-constant stellar mass-to-light ratio (M/L_{F160W}), molecular gas exponential disc scale length (R_0), integrated flux density and velocity dispersion (σ_{gas}), and the "nuisance" disc parameters position angle, inclination (i), systemic velocity (V_{sys}) and centre position (offsets in right ascension and in declination from the image phase centre). The model parameters and their search ranges, best-fitting values and 1σ (68.3 per cent) and 3σ (99.7 per cent) confidence level uncertainties are listed in Table 4.

The final MCMC chain had 200,000 steps. It is clear that there is a massive dark object in the centre of NGC 4751, with a best-fitting mass of $3.43^{+0.45}_{-0.44} \times 10^9 M_{\odot}$, where here and throughout this paper the uncertainties are stated at the 3σ (99.7 per cent) confidence level. The best-fitting M/L in the *F160W* filter is $(2.68 \pm 0.11) M_{\odot}/L_{\odot, F160W}$. Figure 5 also shows a slight degeneracy between M_{BH} and M/L_{F160W} , equivalent to the conservation of (total) dynamical mass (see e.g. Smith et al. 2019 for more details).

The quality of our best-fitting model is easiest to judge by overlaying it over the kinematic major-axis PVD. From left to right in Fig. 7, we thus overlay the best-fitting model with no SMBH, a SMBH and an overly-massive SMBH (≈ 0.2 dex more massive than the best-fitting SMBH), respectively, allowing all parameters other than the SMBH mass to vary in the first and third case. As expected for the best-fitting no SMBH model, a higher stellar M/L is derived

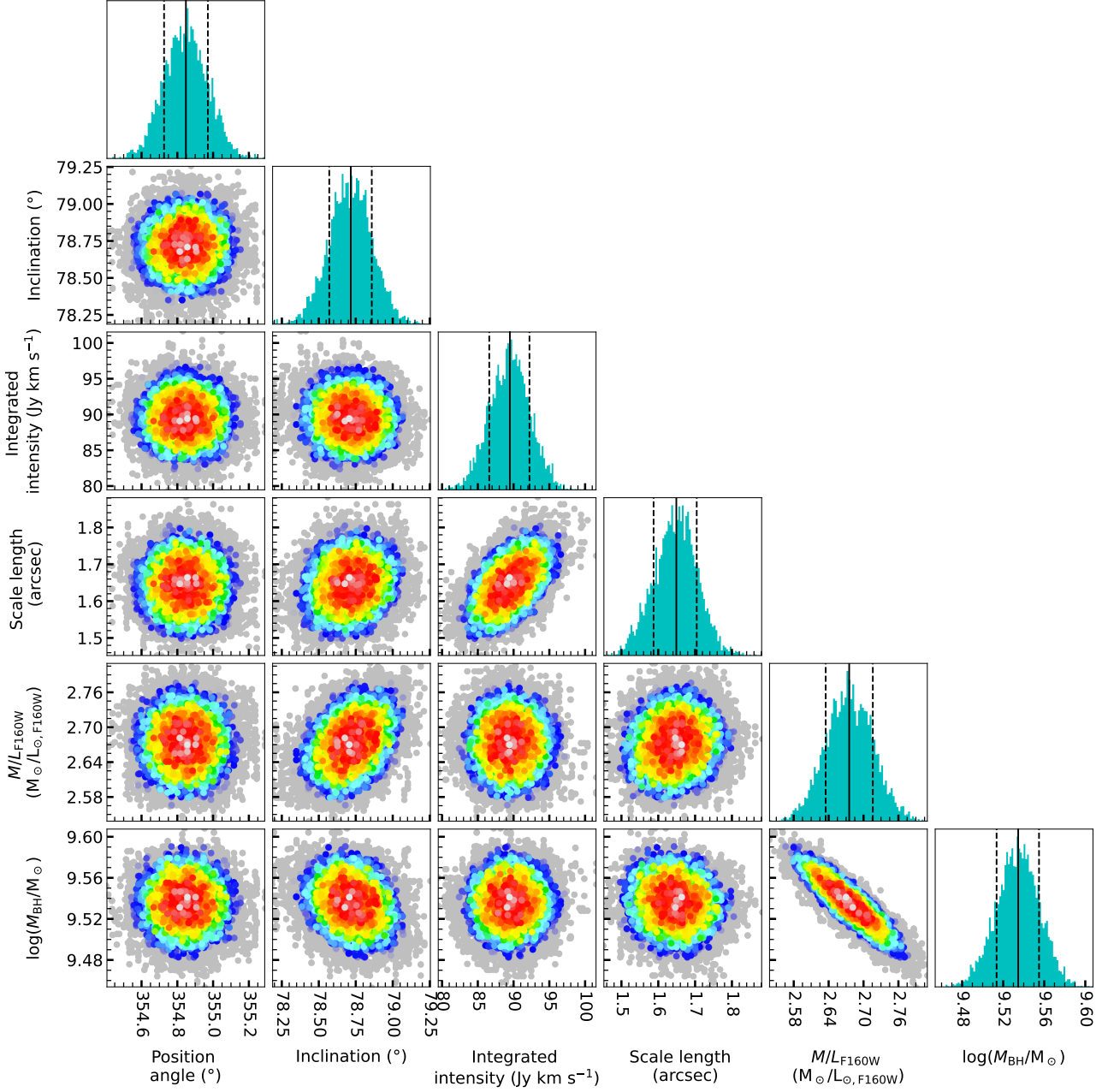


Figure 5. Corner plots of NGC 4751, showing the covariances between selected (primarily non- nuisance) parameters of the constant M/L model. Each data point is one realisation of our model, colour-coded to show the relative log-likelihood of that realisation, with white data points being most likely and blue data points least likely. Coloured data points show models within $\Delta\chi^2 < \sqrt{2N}$ of the best-fitting model; grey data points show all remaining models. The histograms show the 1D marginalised posterior distribution of each model parameter; for each the black solid line indicates the median and the two black dashed lines the 68% confidence interval.

as the model attempts to account for the high rotation velocities at small radii without a SMBH. Nevertheless, the model is unable to reproduce those central velocities without greatly exceeding the relatively low velocities at larger radii. The compromise reached is thus unsatisfactory at both small and large radii. Again as expected, the best-fitting overly-massive SMBH model yields a smaller M/L , but the fit is very poor at small radii, the model over-shooting even the highest velocities. The best-fitting SMBH model not only reproduces the data best, but the fit is very good at all radii and velocities.

4.2.2 Model with linearly-varying M/L

This model has a total of 11 free parameters: a stellar M/L intercept and a stellar M/L gradient replace the constant M/L of the previous model, while the other 9 parameters remain the same. The model parameters and their search ranges, best-fitting values and 1σ and 3σ confidence level uncertainties are listed in Table 4.

The final MCMC chain has 200,000 steps. The model has a best-fitting SMBH mass of $2.79^{+0.75}_{-0.57} \times 10^9 M_\odot$ and a best-fitting M/L in the $F160W$ filter represented by $(M/L_{F160W}) / (M_\odot/L_{\odot,F160W}) = 3.07^{+0.27}_{-0.35} - 0.09^{+0.08}_{-0.06} (R/\text{arcsec})$. Figure 6 again shows a negative

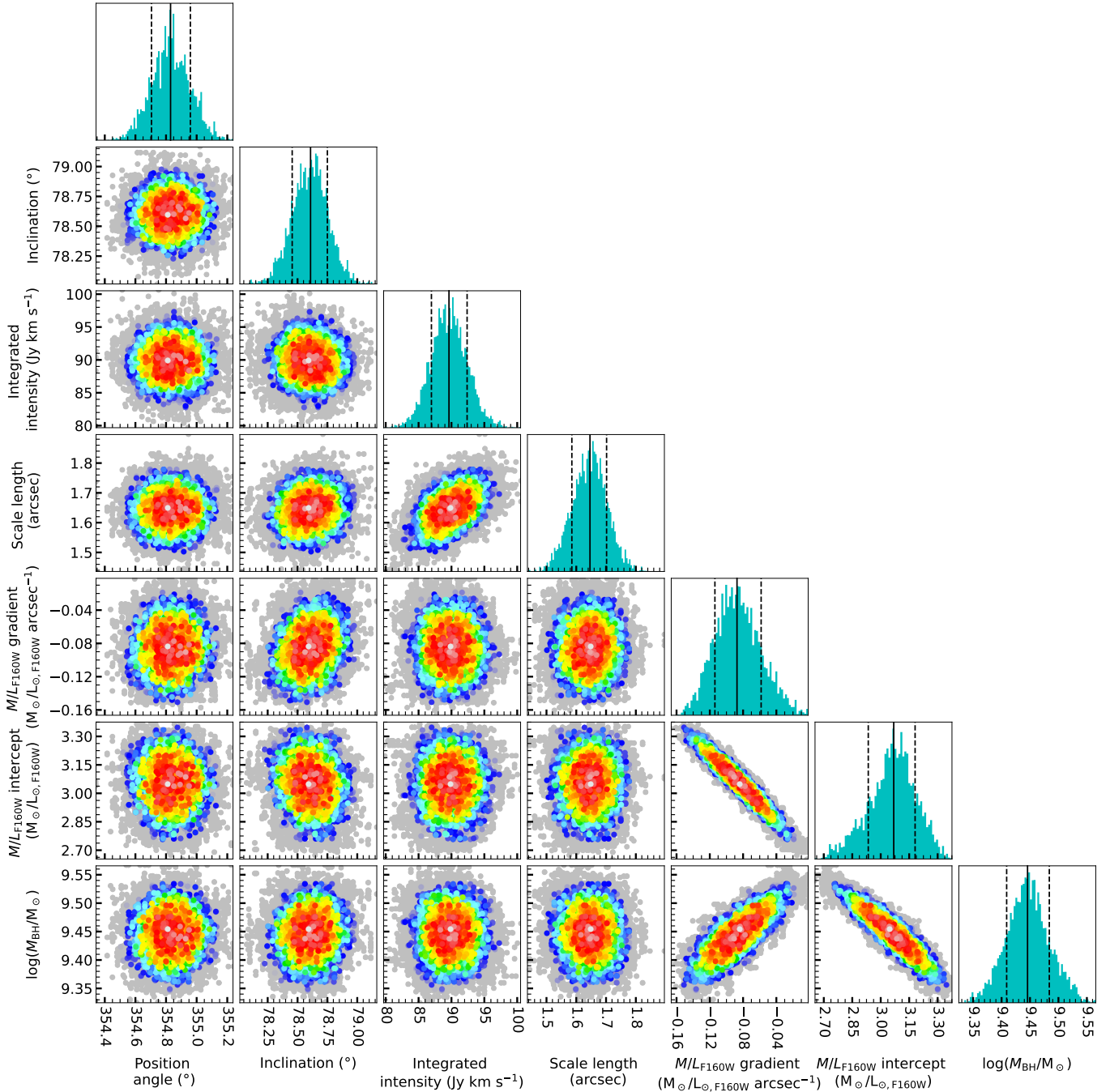


Figure 6. As Fig. 5, but for the model with a radially linearly-varying M/L .

correlation between the M/L intercept (i.e. the M/L in the centre of the galaxy) and the SMBH mass, which is again equivalent to the conservation of (total) dynamical mass. Consequently, there is also a positive correlation between SMBH mass and M/L gradient - as more mass is attributed to the SMBH, the M/L intercept decreases and thus the M/L gradient becomes less negative (to still fit the outer regions of the galaxy well).

As before, the quality of our best-fitting model is easiest to judge by overlaying it over the kinematic major-axis PVD. From left to right in Fig. 8, we overlay the best-fitting model with a linear M/L and no SMBH, a linear M/L and a SMBH, and a linear M/L and an

overly-massive SMBH (≈ 0.2 dex more massive than the best-fitting SMBH), respectively, allowing all parameters other than the SMBH mass to vary in the first and third case. As expected, the best-fitting no SMBH model has a higher M/L intercept, to account for the high rotation velocities at small radii, and a more negative M/L gradient, to attempt to lower the overall M/L and fit the data at large radii. As before, the model fails to reproduce the extremely high central velocities without also exceeding the low velocities at large radii. The best-fitting overly-massive SMBH model yields a significantly smaller M/L intercept, to attribute less dynamical mass to the stellar component. As expected, the M/L gradient is also now positive,

Table 4. Best-fitting molecular gas model parameters and associated uncertainties.

Parameter		Prior		Best fit	1 σ uncertainty	3 σ uncertainty
Model with constant M/L						
Mass model						
$\log(M_{\text{BH}}/M_{\odot})$	7	→	11	9.535	-0.021, +0.020	-0.059, +0.053
Stellar M/L_{F160W} ($M_{\odot}/L_{\odot, F160W}$)	0.0	→	5.0	2.68	±0.04	±0.11
Molecular gas disc						
Inclination ($^{\circ}$)	0.0	→	89.9	78.7	±0.1	-0.5, +0.6
Position angle ($^{\circ}$)	0.0	→	359.9	354.8	±0.1	-0.3, +0.4
Velocity dispersion (km s^{-1})	0.0	→	50.0	15.1	±2.3	-6.7, +6.5
Scale length (arcsec)	0.0	→	5.0	1.65	±0.06	-0.15, +0.16
Nuisance parameters						
Centre RA offset (arcsec)	-5.4	→	5.4	0.03	±0.004	±0.01
Centre Dec. offset (arcsec)	-4.0	→	4.0	0.31	±0.01	±0.02
Systemic velocity (km s^{-1})	1800	→	2400	2094.5	±1.1	-3.3, +2.9
Integrated intensity (Jy km s^{-1})	0.0	→	150.0	89.5	-2.9, +2.8	-7.8, +7.5
Model with linearly-varying M/L						
Mass model						
$\log(M_{\text{BH}}/M_{\odot})$	7	→	11	9.446	-0.037, +0.039	-0.099, +0.103
Stellar M/L_{F160W} intercept ($M_{\odot}/L_{\odot, F160W}$)	0.0	→	5.0	3.07	-0.13, +0.11	-0.35, +0.27
Stellar M/L_{F160W} gradient ($M_{\odot}/L_{\odot, F160W} \text{ arcsec}^{-1}$)	-2.0	→	2.0	-0.09	±0.03	-0.06, +0.08
Molecular gas disc						
Inclination ($^{\circ}$)	0.0	→	89.9	78.6	-0.2, +0.1	-0.5, +0.4
Position angle ($^{\circ}$)	0.0	→	359.9	354.8	±0.1	-0.3, +0.4
Velocity dispersion (km s^{-1})	0.0	→	50.0	14.8	±1.5	-4.3, +4.4
Scale length (arcsec)	0.0	→	5.0	1.65	±0.06	-0.16, +0.15
Nuisance parameters						
Centre RA offset (arcsec)	-5.4	→	5.4	0.03	±0.004	±0.01
Centre Dec. offset (arcsec)	-4.0	→	4.0	0.31	±0.01	±0.02
Systemic velocity (km s^{-1})	1800	→	2400	2094.3	-1.1, +1.0	-4.4, +4.3
Integrated intensity (Jy km s^{-1})	0.0	→	150.0	89.6	-2.7, +2.8	-7.3, +7.8

Note. The RA and Dec. offsets are measured with respect to the image phase centre, $12^{\text{h}}52^{\text{m}}50^{\text{s}}.748$, $-42^{\circ}39'35''.880$ (J2000.0).

as otherwise the low central M/L would lead to undershooting the velocities at large radii. Despite this, the overly-massive SMBH model is unable to reproduce the data satisfactorily. Once again, the best-fitting free SMBH model reproduces the data best, fitting well at all radii and velocities.

5 JAM MODELS OF STELLAR KINEMATICS

We obtained an alternative SMBH mass estimate using the JAM method (Cappellari 2008; Cappellari 2020) and the SINFONI stellar kinematics of NGC 4751 published by Rusli et al. (2013). We first used the WEBPLOTDIGITIZER software⁶ to extract the stellar kinematics (line-of-sight mean velocity V and velocity dispersion σ) from the published paper (Fig. 24 of Rusli et al. 2013). From these, we computed the second velocity moment as $V_{\text{rms}} = \sqrt{V^2 + \sigma^2}$, which can be directly compared to the JAM predictions.

We fitted an image of the SINFONI PSF, kindly provided to us by Jens Thomas, using the `mge_fit_sectors` procedure in the MGEFIT package as before. Two circular Gaussians were sufficient to provide a good representation of the PSF, with best-fitting parameters $\text{FWHM} = [0''.24, 0''.82]$ and $\text{Frac} = [0.55, 0.45]$, where FWHM is the full width at half maximum of the Gaussians and Frac is the fractional light contribution of the two PSF components. As expected

the FWHM of the narrow component is close to the FWHM of $0''.22$ listed in Table 2 of Rusli et al. (2013), while the FWHM of the broad component is similar to typical FWHM measured from similar SINFONI observations (see e.g. Table 3 of Thater et al. 2019).

We adopted the same *HST* WFC3 *F160W* filter MGE parametrisation used to model the molecular gas kinematics in Section 4.1 to describe the stellar surface brightness of the JAM dynamical models. Moreover, we assumed mass-follows-light and constant anisotropy. The latter assumption is unlikely to be accurate over large spatial scales, and in fact our (more spatially extended) CO model indicates an M/L gradient. However, the JAM model is constrained only by the stellar kinematics within $R \lesssim 1''$, so the results are only weakly sensitive to possible M/L gradients outside that region.

To test for systematics in the modelling, we explored the two extreme assumptions for the shape of the velocity ellipsoid: we used either JAM_{cyl} with a cylindrically-aligned velocity ellipsoid (Cappellari 2008), or JAM_{sph} with a spherically-aligned orientation (Cappellari 2020). The anisotropy has a different meaning in the two cases. For JAM_{cyl} , the anisotropy is $\beta_z = 1 - \sigma_z^2/\sigma_R^2$, where σ_z and σ_R are the intrinsic stellar velocity dispersions in the R and z cylindrical coordinates, respectively. For JAM_{sph} , the anisotropy is $\beta_r = 1 - \sigma_{\theta}^2/\sigma_r^2$, where σ_{θ} and σ_r are the intrinsic stellar velocity dispersions in the r and θ spherical coordinates, respectively.

The models have four free parameters: the inclination, which we parametrise (as standard with JAM) with the intrinsic axial ratio q_{min}

⁶ <https://github.com/ankitrohatgi/WebPlotDigitizer>

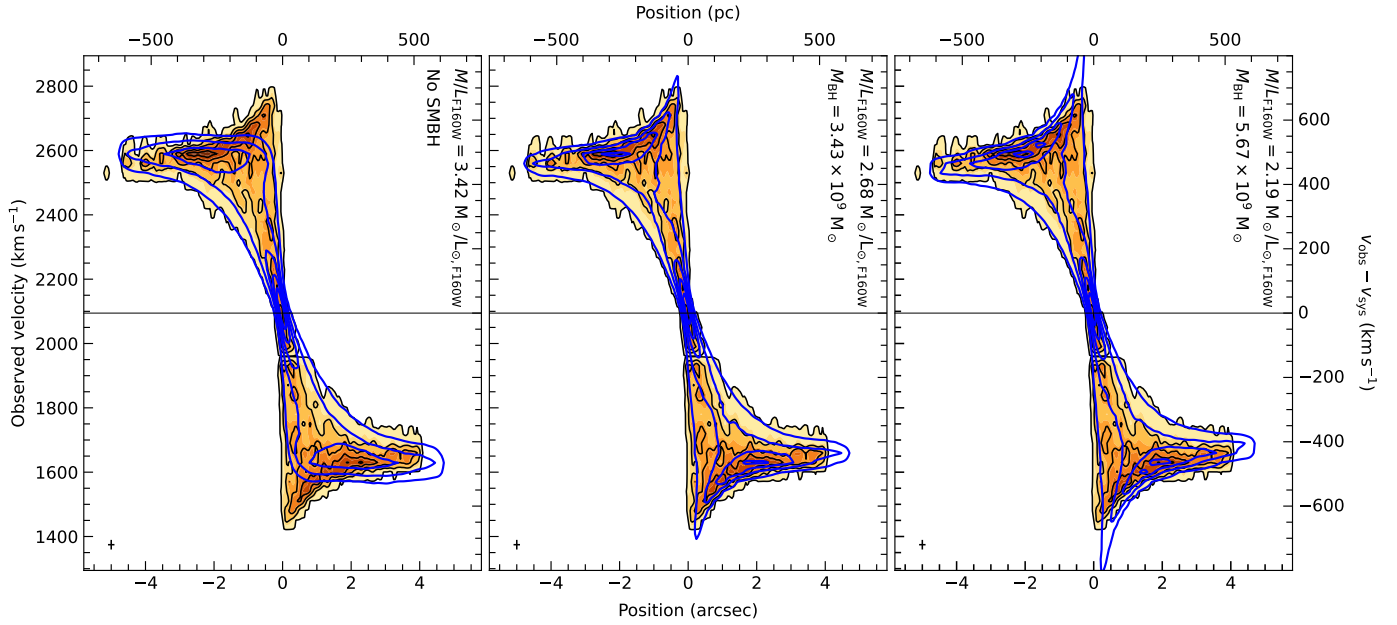


Figure 7. Observed kinematic major-axis PVD of NGC 4751 (orange scale with black contours), overlaid with the best-fitting no SMBH (left), free SMBH mass (centre) and overly-massive (by ≈ 0.2 dex) SMBH (right) model (blue contours), respectively. The SMBH mass and M/L of each model are listed in the top-right corner of each panel. An error bar is shown in the bottom-left corner of each panel, showing the size of the synthesised beam along the kinematic major-axis and the channel width. The need for a central dark mass to fully account for the gas kinematics at all radii is clear.

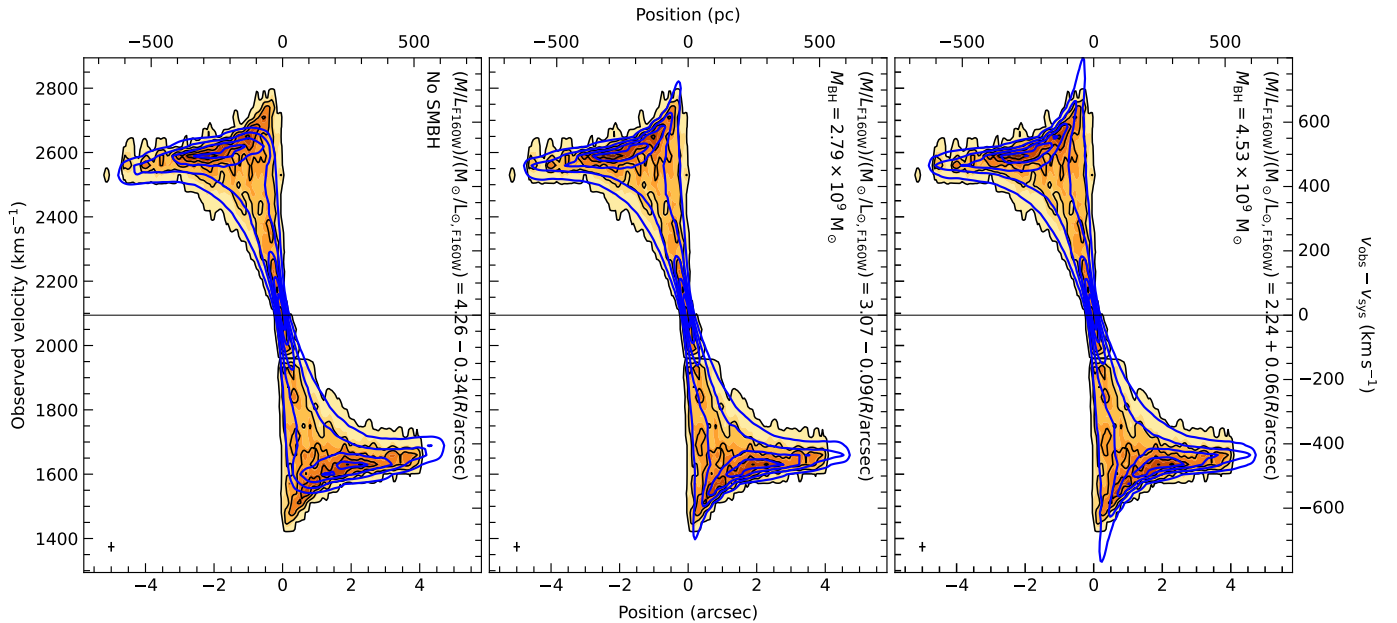


Figure 8. As Fig. 7, but for models with radially linearly-varying M/L .

of the flattest Gaussian of the MGE, the orbital anisotropy β_z or β_r , the SMBH mass M_{BH} and the total mass-to-light ratio $(M/L)_{\text{tot}}$.

One of the key practical differences between the [Schwarzschild \(1979\)](#) dynamical modelling method and JAM is that the former requires large-scale stellar kinematics to provide tight constraints on the SMBH, while the latter works best when the fit is restricted

to the smallest field of view that is sufficiently large to break the degeneracy between M_{BH} and $(M/L)_{\text{tot}}$. This implies that, while with Schwarzschild models it becomes essential to model dark halo variations and M/L gradients, with JAM one can approximate the M/L and anisotropy to be constant within the small region that is used for the fit (see e.g. [Thater et al. 2022](#)).

Table 5. Best-fitting stellar kinematic model parameters and associated uncertainties, approximately accounting for systematics.

Parameter	Best fit	1σ uncertainty	3σ uncertainty
Model with JAM_{cyl}			
M_{BH} ($10^9 M_{\odot}$)	2.52	± 0.12	± 0.36
M/L_{tot} ($M_{\odot}/L_{\odot, F160W}$)	3.76	± 0.09	± 0.28
q_{min}	0.05	± 0.08	± 0.24
β_z	-0.23	± 0.09	± 0.26
Model with JAM_{sph}			
M_{BH} ($10^9 M_{\odot}$)	3.24	± 0.29	± 0.87
M/L_{tot} ($M_{\odot}/L_{\odot, F160W}$)	4.22	± 0.16	± 0.48
q_{min}	0.05	± 0.07	± 0.22
β_r	-3.1	± 2.1	± 6.3

We performed the fits and derived the corresponding formal uncertainties using the CAPFIT least-squares fitting procedure⁷ (see Sec. 4.2 of Cappellari 2023). We started by assigning constant uncertainties $\Delta V_{\text{rms}} = 1 \text{ km s}^{-1}$ to all kinematic measurements and we performed the fit with CAPFIT. This yielded the best-fitting parameters p_j and their formal uncertainties Δp_j (i.e. from the diagonal terms of the covariance matrix at the best fit) at the 1σ confidence level. We then made the common assumption of a good fit (as indicated by our data/model comparison) to rescale the uncertainties in such a way as to obtain $\chi^2/\text{DOF} = 1$, where DOF is the number of degrees of freedom. This is achieved by setting the new formal uncertainties $\Delta p_j \leftarrow \Delta p_j \sqrt{\chi^2/\text{DOF}}$.

Contrary to the case of our CO SMBH determinations in Section 4, here we did not apply the approximated scaling of the uncertainties of Mitzkus et al. (2017) because the crude correction for very large datasets is not justified in this situation. In fact, we are fitting just 35 V_{rms} values and standard statistics can be used. However, this implies that the relative uncertainties between the two BH determinations are not directly comparable.

The results of the JAM fits and the formal statistical uncertainties are shown in Fig. 9. The data-model comparisons are shown along the five angular sectors provided by Rusli et al. (2013). The models fit the data to a high accuracy. To obtain $\chi^2/\text{DOF} = 1$, one must set $\Delta V_{\text{rms}} = 10 \text{ km s}^{-1}$, corresponding to a median random uncertainty on the kinematics of just 2.6 per cent, which is at the expected level from good quality SINFONI data. The best-fitting parameters and their 1σ formal uncertainties are $M_{\text{BH}} = (2.52 \pm 0.12) \times 10^9 M_{\odot}$ and $(M/L)_{\text{tot}} = 3.759 \pm 0.094 M_{\odot}/L_{\odot, F160W}$ for JAM_{cyl}, and $M_{\text{BH}} = (3.24 \pm 0.29) \times 10^9 M_{\odot}$ and $(M/L)_{\text{tot}} = 4.22 \pm 0.16 M_{\odot}/L_{\odot, F160W}$ for JAM_{sph}. These best-fitting parameters are remarkably consistent with those obtained from our molecular gas modelling (see Section 4.2) and are summarised in Table 5. The best-fitting inclination for both JAM models is $i \approx 72^\circ$, also close to that derived from the molecular gas kinematics.

6 DISCUSSION

6.1 Best-fitting molecular gas mass models

In this paper we presented molecular gas mass models with two different M/L profiles. As can be seen in Figs. 7 and 8, the two models provide near-identical fits visually. We can judge the goodness-of-fit of the models more robustly by using the reduced χ^2 statistic χ_{red}^2 . The best-fitting CO model with a constant M/L has $\chi_{\text{red}}^2 = 2.49$,

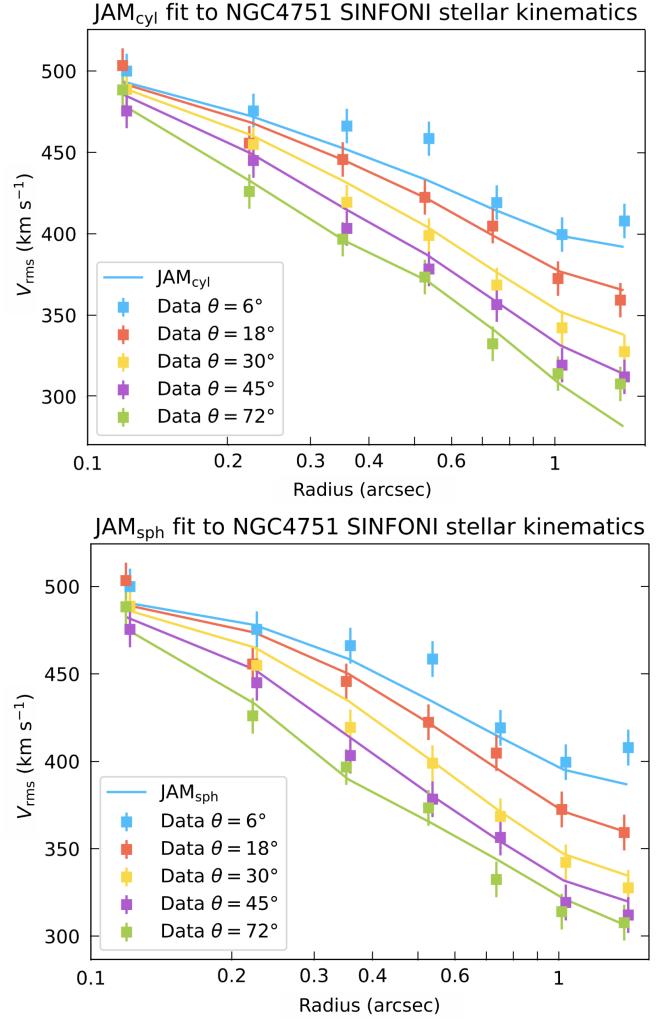

Figure 9. JAM_{cyl} (top) and JAM_{sph} (bottom) modelling of the SINFONI stellar kinematics from Rusli et al. (2013). The data are shown for five angular sectors (as indicated) centred on the galaxy nucleus. The uncertainties are scaled to yield $\chi^2/\text{DOF} = 1$.

Table 6. χ^2 of the models discussed.

Model	χ_{red}^2	k	BIC
(1)	(2)	(3)	(4)
Best-fitting CO model with constant M/L	2.49	10	610
Best-fitting CO model with linearly-varying M/L	2.43	11	609

Notes. (1) Model. (2) Reduced χ^2 statistic. (3) Number of free parameters. (4) Bayesian information criterion.

while the best-fitting CO model with a radially linearly-varying M/L has $\chi_{\text{red}}^2 = 2.43$. However, as these models have different numbers of free parameters, it is preferable to use the Bayesian information criterion $\text{BIC} \equiv k \ln N - 2 \ln P$ to compare them, where k is the number of free parameters of each model and N and $\ln P$ are as defined in Section 4.1. The BIC difference between the two best-fit CO models presented in this paper is $\Delta \text{BIC} \approx 1$, so they are equally good fit. These results are summarised in Table 6.

Figures 10 and 11 show the cumulative mass distribution of NGC 4751 for the model with a constant M/L and the model with a radially linearly-varying M/L , respectively. Using the standard definition of a SMBH SoI (see Section 2) and the best-fitting SMBH

⁷ <https://pypi.org/project/ppxf/>

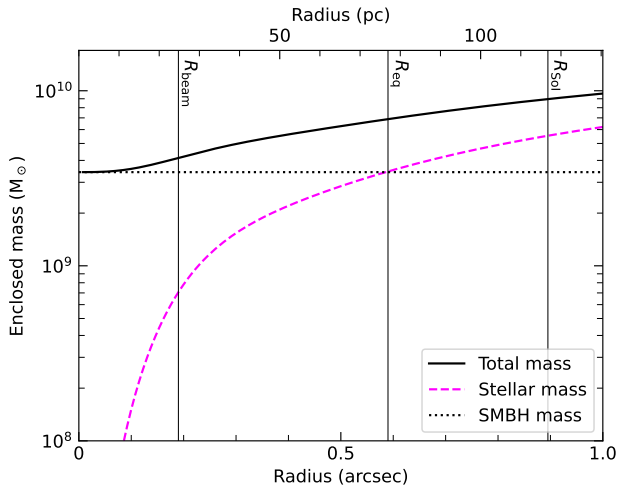


Figure 10. Cumulative mass function of NGC 4751 for the model with a constant M/L , showing the relative contributions of the SMBH (black dotted line) and stars (magenta dashed line) to the total enclosed mass (black solid line). The three vertical black lines indicate the physical extent of the synthesised beam (R_{beam}), the radius of the SMBH sphere of influence (R_{SoI} , assuming $\sigma_e = 355.4 \text{ km s}^{-1}$ and our best-fitting SMBH mass) and the radius of equal mass contribution (R_{eq}).

mass for the constant M/L model yields $R_{\text{SoI}} \approx 116 \text{ pc}$ ($\approx 0.89 \text{ arcsec}$), whereas the best-fitting SMBH mass for the linear M/L model yields $R_{\text{SoI}} \approx 95 \text{ pc}$ ($\approx 0.73 \text{ arcsec}$). Both of these are significantly larger than the size of the synthesised beam. One can also assess the impact of a SMBH by considering the radius at which the enclosed stellar mass is equal to that of the SMBH. Figure 10 shows this radius of equal mass contribution to be $R_{\text{eq}} \approx 77 \text{ pc}$ ($\approx 0.59 \text{ arcsec}$), smaller than the usual R_{SoI} , but still significantly larger than the size of the synthesised beam. Figure 11 shows the radius of equal mass contribution to be $R_{\text{eq}} \approx 59 \text{ pc}$ ($\approx 0.45 \text{ arcsec}$), also smaller than the usual R_{SoI} , but still more than twice the size of the synthesised beam. In fact, in both models the SMBH dominates the potential so significantly that at the innermost radius probed (the radius equal to the size of the synthesised beam, $R_{\text{beam}} \approx 82$ per cent of the enclosed mass is due to the SMBH in the constant M/L model and ≈ 76 per cent in the linear M/L model, making the SMBH mass determination trivial in both models.

The quality of our SMBH measurement can be assessed in terms of how well resolved the SMBH SoI is and the proximity of our dynamical tracer to the SMBH. In the region dominated by the SMBH, Zhang et al. (2024) derive a simple relation between the highest circular velocity measured v_c and the innermost radius probed R_{min} , where R_{min} can be normalised by respectively R_{SoI} , R_{eq} and the Schwarzschild radius $R_{\text{Schw}} \equiv 2GM_{\text{BH}}/c^2$, where c is the speed of light. The resulting relations allow to compare the spatial resolutions of different datasets and the sizes of the regions probed in a M_{BH} -independent manner. Our observations of NGC 4751 detect a maximum line-of-sight velocity $v_{\text{obs}} \approx 687 \text{ km s}^{-1}$ (see e.g. Fig. 7). Deprojecting this velocity using $v_c = v_{\text{obs}}/\sin i$, where $i = 78^\circ.7$ (Table 4), the highest circular velocity probed is $\approx 700 \text{ km s}^{-1}$. This is the second highest circular velocity ever probed by a molecular gas measurement, rivaled only by the high-resolution measurement of NGC 0383 (Zhang et al. in prep.). With a spatial resolution of $\approx 26 \text{ pc}$ ($\approx 0.20 \text{ arcsec}$), our measurement of NGC 4751 probes material down to $R_{\text{min}}/R_{\text{Schw}} \approx 83,000$, $R_{\text{min}}/R_{\text{SoI}} \approx 0.23$ and $R_{\text{min}}/R_{\text{eq}} \approx 0.33$

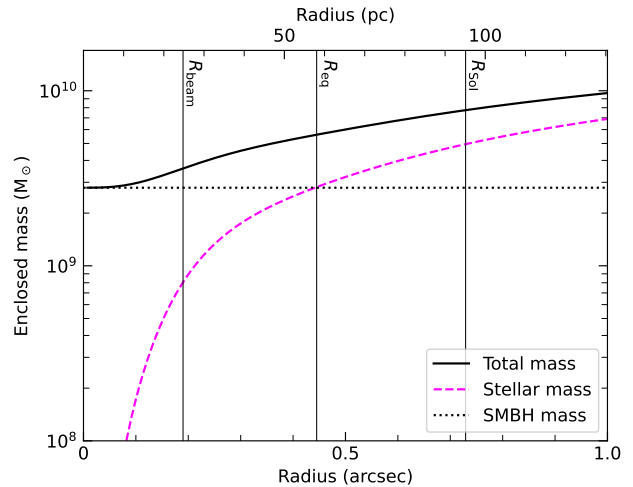


Figure 11. As Fig. 10, but for the model with a radially linearly-varying M/L .

for the model with a constant M/L , and $R_{\text{min}}/R_{\text{Schw}} \approx 101,000$, $R_{\text{min}}/R_{\text{SoI}} \approx 0.28$ and $R_{\text{min}}/R_{\text{eq}} \approx 0.46$ for the model with a radially linearly-varying M/L .

6.2 Molecular gas-derived SMBH mass uncertainties

Aside from the fitting uncertainties listed in Table 4, our molecular gas measurements are subject to several other potential sources of systematic error. The first of these is the distance. For all dynamical mass measurements, $M_{\text{BH}} \propto D$, so the adopted distance affects the SMBH mass linearly. Conversely, the inferred SMBH mass can be re-scaled for any adopted distance. As standard, the distance uncertainties are neither quoted nor propagated into our SMBH mass measurement, but these are typically about 20 – 30 per cent when flow models are applied to relatively nearby galaxies ($D < 50 \text{ Mpc}$; Lelli et al. 2016).

In our modelling we have only considered the mass contributions of the stars and SMBH, and have assumed the dark matter and molecular gas to have negligible masses. The spatial scales over which dark matter effects are significant are much greater than those considered in this paper and those where the SMBH dominates the potential. In the very unlikely scenario that there is significant diffuse dark matter in the central regions, its contribution to the circular velocity is expected to increase with radius similarly to that of the stars, whereas the contribution of the SMBH declines in a Keplerian fashion (see e.g. Fig. 7 of Lelli et al. 2022). Thus, the dark matter contribution is most strongly degenerate with that of the stars, which would lead to a different best-fitting M/L without strongly affecting the SMBH mass. Furthermore, Rusli et al. (2013) considered models of NGC 4751 with and without dark matter, and there was no significant difference in the SMBH masses inferred, with only a minor impact on the M/L (see Section 2). Similarly, as discussed in Section 3.1, NGC 4751 has an extended molecular gas distribution with a total mass of $(3.17 \pm 0.07) \times 10^8 M_\odot$, which if plotted would not even be visible in Fig. 10 (as the total mass is only reached at the outer edge of the disc). The contribution of molecular gas is thus negligible compared to those of the stars and SMBH.

6.3 Comparison of stellar kinematics results

As discussed in Section 2, prior to our JAM models, Rusli et al. (2013) used the same SINFONI data to infer a SMBH mass of

$(1.4 \pm 0.1) \times 10^9 M_{\odot}$ at 1σ (68 per cent) confidence level, modelled using three-integral Schwarzschild models assuming the same distance as us. Unlike our JAM model SMBH masses, the mass in Rusli et al. (2013) is not consistent with our molecular gas and JAM SMBH masses.

Part of the disagreement may stem from a potential underestimation of uncertainties in the Rusli et al. (2013) determination. Upon examining their Figure 11, we note that the $\Delta\chi^2$ line exhibits multiple minima. The primary minimum corresponds to the formally best-fitting solution, with a black hole mass of approximately $1.4 \times 10^9 M_{\odot}$, as reported in their paper. However, there is a secondary minimum at $1.8 \times 10^9 M_{\odot}$, lying outside the formal 3σ confidence interval. This secondary minimum likely arises from numerical noise, a common feature of the Schwarzschild (1979) dynamical modelling method. It is also the reason why the associated $\Delta\chi^2$ values are sometimes smoothed before determining confidence intervals (see e.g. Gebhardt et al. 2003).

The sharp global minimum may indeed be an artifact of numerical noise. By examining the figure, we can speculate that a more realistic uncertainty would encompass the region where the $\Delta\chi^2$ profile sharply rises. This would correspond to a black hole mass range of approximately $[1.1, 2.0] \times 10^9 M_{\odot}$ (3σ limits). If this were the true confidence interval of the Rusli et al. (2013) models, it would significantly reduce, although not eliminate, the tension between their results and ours.

6.4 The $M_{\text{BH}} - \sigma$ relation: comparison to the literature

As outlined in Section 1, SMBH masses are often considered within the context of host galaxy – SMBH mass correlations, that aid our understanding of their (co-)evolution. We thus compare our NGC 4751 SMBH mass measurements to the $M_{\text{BH}} - \sigma_e$ relation of van den Bosch (2016). Despite being $\approx 2.0 - 2.5$ times larger than the mass inferred by Rusli et al. (2013), both of our SMBH mass measurements inferred using the molecular gas method are still slightly under-massive given NGC 4751’s stellar velocity dispersion, although both are well within the scatter of the relation. Likewise, our stellar kinematic SMBH masses are still slightly under-massive but within the scatter of the $M_{\text{BH}} - \sigma_e$ relation.

However, the discrepancy between our SMBH mass measurements and those of Rusli et al. 2013 highlight a long-standing issue in the study of SMBHs and host galaxy – SMBH mass correlations. There are differences between SMBH masses determined using different kinematic tracers, but also between SMBH masses determined using the same tracer but different modelling methods/assumptions. Ideally, all these methods should be cross-checked against maser measurements, generally considered the gold standard of SMBH mass determination, to determine the accuracy and potential biases of the methods. However, the rarity of masers and their strong bias towards relatively low-mass active galaxies (with correspondingly light SMBHs) makes such a comparison impossible in most cases. Instead, one must use the $M_{\text{BH}} - \sigma_e$ relation itself as a proxy to ascertain whether other methods of SMBH mass determination are robust.

Aside from the dwarf galaxy NGC 404, that has a SMBH mass of $< 10^6 M_{\odot}$, there are currently only five galaxies with both a molecular gas and a stellar kinematic SMBH mass measurement: NGC 524 (Krajnović et al. 2009; Smith et al. 2019), NGC 1332 (Rusli et al. 2010; Barth et al. 2016), NGC 4697 (Schulze & Gebhardt 2011; Davis et al. 2017a), NGC 6861 (Rusli et al. 2013; Kabasares et al. 2022) and now NGC 4751 (Rusli et al. 2013 and this paper). Figure 12 compares the stellar (left panel) and molecular gas (right

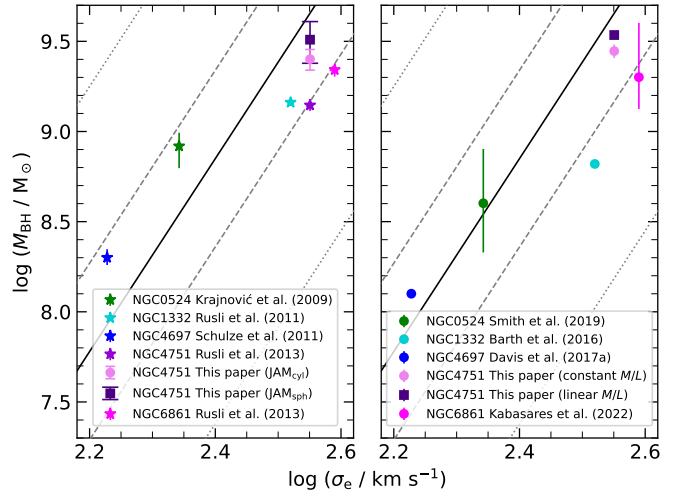


Figure 12. Best-fitting black hole mass – stellar velocity dispersion relation (black line) of van den Bosch (2016), with SMBH masses derived using both stellar kinematics (left) and molecular gas kinematics (right). Dashed and dotted grey lines show the 1σ and 3σ scatter of the relation, respectively. Error bars indicate 3σ confidence level uncertainties for Krajnović et al. (2009) and Smith et al. (2019), 1σ uncertainties otherwise.

panel) kinematic measurements of the SMBH masses of these five objects. Whilst on average the molecular mass measurements tend to lie closer to the $M_{\text{BH}} - \sigma_e$ relation, three of the five galaxies have SMBH masses that are entirely consistent between the two methods (NGC 524, NGC 4751 and NGC 6861).

Despite no clear trend with respect to the $M_{\text{BH}} - \sigma_e$ relation, we can see in Fig. 13 that molecular gas kinematics seems to yield systematically lower SMBH mass estimates than stellar kinematics. It is hard to establish whether the stellar kinematic modelling overestimates the masses or the molecular gas modelling underestimates the masses, but molecular gas modelling is generally considered to be a lot simpler. The main assumption underlying molecular gas modelling is the presence of circular motions, which can be easily verified from the data themselves. Subsequently, the modelling relatively straightforward and has considerable flexibility for implementing position angle and/or inclination warps. Both JAM and Schwarzschild modelling cannot rely on the simple assumption that the tracer population lies on a simple thin disk and they have to fit for the velocity anisotropy of the stars. However, the stars, unlike the gas, have the advantage of being unaffected by non-gravitational forces, like outflows. Both CO and stellar methods can easily model radial M/L gradients. Overall, more cross checks are needed to reach a conclusion on the reliability and possible biases of different methods.

7 CONCLUSIONS

High angular resolution ALMA observations were obtained and used to create a $^{12}\text{CO}(3-2)$ cube of the ETG galaxy NGC 4751. We presented dynamical models with two different M/L radial profiles: constant and linearly varying. We estimated the stellar mass distribution using a MGE model of a *HST* image and each of the M/L profiles, and then forward modelled the molecular gas distribution and kinematics using KINMS and an MCMC framework. NGC 4751 has a regularly-rotating molecular gas disc with an inferred SMBH mass of $3.43^{+0.45}_{-0.44} \times 10^9 M_{\odot}$ and a stellar $F160W$ filter M/L of $(2.68 \pm 0.11) M_{\odot}/L_{\odot, F160W}$ when assuming a constant

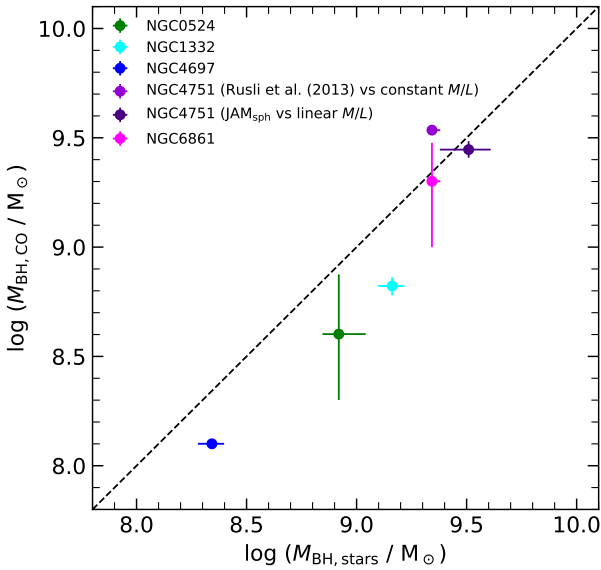


Figure 13. Cross comparison of SMBH masses derived using stellar kinematics and molecular gas. For clarity we have only included two data points for NGC 4751, representing the two extremes. One data point compares the least massive stellar kinematic mass estimate (Rusli et al. 2013) and our most massive molecular gas mass estimate (our model with constant M/L); the other data point compares the most massive stellar kinematic mass estimate (our model assuming JAM_{sph}) and our least massive molecular gas mass estimate (our model with linearly-varying M/L). All data points comparing any other two methods would lie between those two. Error bars are as in Fig. 12.

M/L , and a SMBH mass of $2.79^{+0.75}_{-0.57} \times 10^9 M_{\odot}$ and a stellar $F160W$ filter M/L of $(M/L_{F160W}) / (M_{\odot}/L_{\odot,F160W}) = 3.07^{+0.27}_{-0.35} - 0.09^{+0.08}_{-0.06}$ (R/arcsec) when assuming a linearly-varying M/L (all uncertainties at 3σ confidence levels). We additionally presented stellar kinematic SMBH mass estimates using the JAM method and SINFONI stellar kinematics. Assuming JAM_{cyl} we obtained $M_{BH} = (2.52 \pm 0.36) \times 10^9 M_{\odot}$, while assuming JAM_{sph} we obtained $M_{BH} = (3.24 \pm 0.87) \times 10^9 M_{\odot}$. All of our masses are consistent with each other, but they are inconsistent with and larger than the previous stellar kinematic measurements of Rusli et al. (2013), obtained using Schwarzschild (1979) orbit-superposition method. All of our SMBH masses are consistent with that predicted by the $M_{BH} - \sigma_e$ relation of van den Bosch (2016). We conclude that the best-fitting SMBH mass of Rusli et al. (2013) is strongly excluded by our observations.

ACKNOWLEDGEMENTS

PD acknowledges support from a Science and Technology Facilities Council (STFC) DPhil studentship under grant ST/S505638/1. MB was supported by STFC consolidated grant ‘‘Astrophysics at Oxford’’ ST/K00106X/1 and ST/W000903/1. TAD and IR acknowledge support from STFC grant ST/S00033X/1. This paper makes use of the following ALMA data: ADS/JAO.ALMA 2015.1.01135.S. ALMA is a partnership of ESO (representing its member states), NSF (USA), and NINS (Japan), together with NRC (Canada), MOST and ASIAA (Taiwan), and KASI (Republic of Korea), in cooperation with the Republic of Chile. The Joint ALMA Observatory is operated by ESO, AUI/NRAO, and NAOJ. This research made use of the NASA/IPAC Extragalactic Database (NED), which is operated by the Jet Propul-

sion Laboratory, California Institute of Technology, under contract with the National Aeronautics and Space Administration.

DATA AVAILABILITY

The observations underlying this article are available in the ALMA archive, at <https://almascience.eso.org/asax/>, and in the Hubble Science Archive, at <https://hst.esac.esa.int/ehst/>.

REFERENCES

- Barth A. J., Boizelle B. D., Darling J., Baker A. J., Buote D. A., Ho L. C., Walsh J. L., 2016, *ApJ*, 822, L28
- Boizelle B. D., Barth A. J., Walsh J. L., Buote D. A., Baker A. J., Darling J., Ho L. C., 2019, *ApJ*, 881, 10
- Boizelle B. D., et al., 2021, *ApJ*, 908, 19
- Campbell L. A., et al., 2014, *MNRAS*, 443, 1231
- Cappellari M., 2002, *MNRAS*, 333, 400
- Cappellari M., 2008, *MNRAS*, 390, 71
- Cappellari M., 2020, *MNRAS*, 494, 4819
- Cappellari M., 2023, *MNRAS*, 526, 3273
- Cappellari M., et al., 2013, *MNRAS*, 432, 1709
- Cohn J. H., et al., 2021, *ApJ*, 919, 77
- Dame T. M., 2011, preprint, ([arXiv:1101.1499](https://arxiv.org/abs/1101.1499))
- Davis T. A., et al., 2013a, *MNRAS*, 429, 534
- Davis T. A., Bureau M., Cappellari M., Sarzi M., Blitz L., 2013b, *Nature*, 494, 328
- Davis T. A., Bureau M., Onishi K., Cappellari M., Iguchi S., Sarzi M., 2017a, *MNRAS*, 468, 4675
- Davis T. A., et al., 2017b, *MNRAS*, 473, 3818
- Davis T. A., et al., 2020, *MNRAS*, 496, 4061
- Davis T. A., et al., 2022, *MNRAS*, 512, 1522
- Dominiak P., Bureau M., Davis T. A., Ma C.-P., Greene J. E., Gu M., 2024, *MNRAS*, 529, 1597
- Ferrarese L., Ford H. C., Jaffe W., 1996, *ApJ*, 470, 444
- Gebhardt K., et al., 2000, *ApJ*, 539, L13
- Gebhardt K., et al., 2003, *ApJ*, 583, 92
- Gerhard O. E., Binney J. J., 1996, *MNRAS*, 279, 993
- Gültekin K., et al., 2009, *ApJ*, 698, 198
- Hopkins P. F., Cox T. J., Younger J. D., Hernquist L., 2009, *ApJ*, 691, 1168
- Huang S., Ho L. C., Peng C. Y., Li Z.-Y., Barth A. J., 2013, *ApJL*, 768, L28
- Kabasares K. M., et al., 2022, *ApJ*, 934, 162
- Kormendy J., Ho L. C., 2013, *ARA&A*, 51, 511
- Kormendy J., Fisher D. B., Cornell M. E., Bender R., 2009, *ApJS*, 182, 216
- Krajnović D., McDermid R. M., Cappellari M., Davies R. L., 2009, *MNRAS*, 399, 1839
- Krist J. E., Hook R. N., Stoehr F., 2011, in Proc. SPIE, 8127, 81270J.
- Lelli F., McGaugh S. S., Schombert J. M., 2016, *AJ*, 152, 157
- Lelli F., Davis T. A., Bureau M., Cappellari M., Liu L., Ruffa I., Smith M. D., Williams T. G., 2022, *MNRAS*, 516, 4066
- Leroy A. K., et al., 2022, *ApJ*, 927, 149
- Liang F.-H., et al., 2023, *MNRAS*, 527, 9343
- Magorrian J., et al., 1998, *AJ*, 115, 2285
- McConnell N. J., Ma C.-P., 2013, *ApJ*, 764, 184
- McMullin J. P., Waters B., Schiebel D., Young W., Golap K., 2007, in ASP Conf. Ser. Vol. 376, *Astronomical Data Analysis Software and Systems XVI*, p. 127
- Mihos J. C., Hernquist L., 1994, *ApJ*, 431, L9
- Mitzkus M., Cappellari M., Walcher C. J., 2017, *MNRAS*, 464, 4789
- Nagai H., et al., 2019, *ApJ*, 883, 193
- Nguyen D. D., et al., 2017, *ApJ*, 836, 237
- Nguyen D. D., et al., 2020, *ApJ*, 892, 68
- Nguyen D. D., et al., 2021, *MNRAS*, 504, 4123
- North E. V., et al., 2019, *MNRAS*, 490, 319
- Onishi K., Iguchi S., Sheth K., Kohno K., 2015, *ApJ*, 806, 39

- Onishi K., Iguchi S., Davis T. A., Bureau M., Cappellari M., Sarzi M., Blitz L., 2017, *MNRAS*, 468, 4663
- Ruffa I., et al., 2019, *MNRAS*, 489, 3739
- Ruffa I., et al., 2023, *MNRAS*, 522, 6170
- Rusli S. P., Thomas J., Erwin P., Saglia R. P., Nowak N., Bender R., 2010, *MNRAS*, 410, 1223
- Rusli S. P., et al., 2013, *AJ*, 146, 45
- Sahu N., Graham A. W., Davis B. L., 2019, *ApJ*, 876, 155
- Sahu K. C., Anderson J., Baggett S., 2021, WFC3 Data Handbook, v5.0, <https://hst-docs.stsci.edu/wfc3dhh>
- Schlafly E. F., Finkbeiner D. P., 2011, *ApJ*, 737, 103
- Schulze A., Gebhardt K., 2011, *ApJ*, 729, 21
- Schwarzschild M., 1979, *ApJ*, 232, 236
- Smith M. D., et al., 2019, *MNRAS*, 485, 4359
- Smith M. D., et al., 2021, *MNRAS*, 503, 5984
- Thater S., Krajnović D., Cappellari M., Davis T. A., de Zeeuw P. T., McDermid R. M., Sarzi M., 2019, *A&A*, 625, A62
- Thater S., et al., 2022, *MNRAS*, 509, 5416
- Willmer C. N. A., 2018, *ApJSS*, 236, 47
- Zhang H., et al., 2024, *MNRAS*, submitted
- van den Bosch R. C. E., 2016, *ApJ*, 831, 134
- van den Bosch R. C. E., van de Ven G., 2009, *MNRAS*, 398, 1117
- van der Marel R. P., van den Bosch F. C., 1998, *AJ*, 116, 2220

This paper has been typeset from a \TeX/L\AA\TeX file prepared by the author.